Article:
Li, P. and Maiden, A. orcid.org/0000-0002-8192-8235 (2018) Lensless LED matrix ptychographic microscope: problems and solutions. Applied Optics, 57 (8). pp. 1800-1806. ISSN 1559-128X

https://doi.org/10.1364/AO.57.001800

A lensless LED matrix ptychographic microscope: problems and solutions

PENG LI[1,*] AND ANDREW MAIDEN[1]

[1] Department of Electronic and Electrical Engineering, University of Sheffield, Sheffield, S1 3JD, UK
[*] Corresponding author: peng.li.shef@sheffield.ac.uk

Compiled January 25, 2018

In this paper, a lensless microscope based on ptychography is presented. It disposes of the mechanic movement necessary for conventional ptychography, instead using an LED matrix to obtain a diverse set of diffraction data. This data is subject to multiple experimental factors that deviate from the standard version of ptychography: namely imprecise knowledge of the LED positions, partial temporal and spatial coherence, and varying brightness and illumination distribution between individual LEDs. Despite these difficulties, we show here that the diversity in the ptychographic data allows an iterative phase retrieval algorithm to recover excellent, high resolution images of a resolution test target and a biological sample.

OCIS codes: (100.5070) Phase retrieval; (110.1758)Computational imaging; (170.3010) Image reconstruction techniques.

http://dx.doi.org/10.1364/ao.XX.XXXXXX

1. INTRODUCTION

Lensless imaging is gaining popularity in various applications because of its simplicity, cost-effectiveness and compactness compared to conventional lens-based imaging [1]. Diffraction limited resolution is achievable via lensless imaging, because all the aberrations associated with lenses are not involved. Another big advantage of lensless imaging is access to the phase information, which provides much better contrast than a conventional brightfield intensity image, especially for weakly scattering biological samples where it enables non-invasive label-free imaging [2]. Moreover, unlike the phase contrast provided by Zernike phase contrast microscopy [3] or Nomarski differential interference contrast microscopy [4], the phase information provided by lensless imaging linearly corresponds to optical path length variations within the specimen, allowing quantitative analysis [5].

However, without a lens to form the image, only indirect spatial information from the specimen, i.e. its diffraction pattern, can be detected. A phase retrieval algorithm is necessary in order to invert this diffraction data and recover a specimen image. A particularly successful type of algorithm is the iterative phase retrieval algorithm pioneered by Gerchberg and Saxton (GS algorithm) [6] and improved by Fienup (ER and HIO algorithms) [7][8]. However, since they use only a single diffraction pattern, these algorithms are poorly conditioned and suffer serious convergence problems. Imaging techniques using multiple measurements [9][10][11] are therefore emerging as a solution. Among them, ptychography has become very popular recently [11]. However, it requires to scan the specimen over a coherent illumination patch, which is normally enabled by a mechanic stage, which increases the cost and the complexity of the imaging system, slows down the imaging process, and inevitably perturbs the specimen.

Here we introduce a ptychography-based lensless imaging modality that uses a LED matrix and an aperture with no mechanic movement involved, as shown in Fig. 1. Given that the LEDs are far enough away from the aperture, different LED will produce a plane wave of a different tilt angle at the aperture. Each of the plane waves will cast a different illumination patch through the aperture onto a different region of the specimen. The resulting diffraction pattern is then captured by a digital camera placed downstream. To make full use of the dynamic range of the camera, a diffuser (randomly scattering medium) is placed on top of the aperture to introduce a range of random angles into the beam. Another benefit of using diffuser in the intensity measurement is the improvement of phase retrieval results [12][13]. The measured diffraction patterns are then fed into a phase retrieval algorithm to produce the complex (both modulus and phase) image of the specimen.

Compared to the usual form of ptychography, where a single, highly coherent source is employed, our use of an LED array introduces numerous experimental challenges. The LEDs are both spatially and temporally partially coherent, their emission patterns vary, and their locations are not precisely known. It is therefore remarkable that the diversity in our recorded data allows a phase retrieval process that accommodates all of these experimental factors and produce high resolution, clean images

of our samples. We present the basic ptychographic algorithm in Section 2, and show in Section 3 that its assumptions about the experimental conditions (perfect coherence etc.) lead to poor imaging performance. A demonstration image of a biological sample is given in Section 4 and the conclusions are drawn in Section 5.

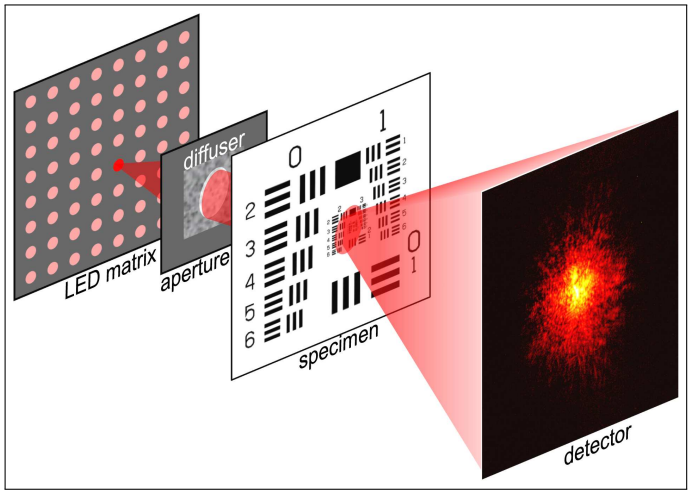

Fig. 1. The experimental geometry of the proposed imaging method.

2. THE RECONSTRUCTION ALGORITHM

The basis of our reconstruction process uses the multi-slice ptychographic reconstruction algorithm commonly used for 3D specimen reconstruction [14]. The detailed procedures of the reconstruction algorithm designed specifically for the proposed imaging method are as follows:

1. Choose the diffraction pattern measured from the LED that is aligned with the optical axis of the imaging system as the reference $I_{\text{ref}}(\mathbf{u})$ and cross correlate it with all the measured diffraction patterns to find out the relative shifts between them

$$\triangle \mathbf{u}_j = \max_{\triangle \mathbf{u}} \left\{ \sum_{\mathbf{u}} I_{\text{ref}}(\mathbf{u}) I_j(\mathbf{u} + \triangle \mathbf{u}) \right\}. \tag{1}$$

   Here $\mathbf{u}$ is the coordinate in diffraction plane and j indexes the LEDs. It should be noted that this step relies on the specimen being weakly scattering. However, even when the specimen is strongly scattering, we can always measure a set of diffraction patterns without the specimen in the beam and use this step to find the incidence angle of all the LEDs beforehand.

2. Use the relative shifts to model the plane waves corresponding to the illumination from each LED:

$$\Gamma_j(\mathbf{r}) = \exp\left[i2\pi \left(\frac{\triangle \mathbf{u}_j}{M} \mathbf{r} \right) \right]. \tag{2}$$

   Here $\mathbf{r}$ denotes the coordinate in real space plane, $i^2 = -1$ and M is the pixel number of the calculation window size.

3. Pass one plane wave through rough initial estimates of the aperture and diffuser (together represented by $A(\mathbf{r})$) and propagate to the specimen plane, giving the illumination function

$$P_j^n(\mathbf{r}) = \wp_{\triangle z} \Big\{ \Gamma_j(\mathbf{r}) A^n(\mathbf{r}) \Big\}. \tag{3}$$

   Here $\wp_{\triangle z}$ represents the propagation over a distance $\triangle z$ and n denotes the iteration number. Since here the distance $\triangle z$ is a very small value, we used angular spectrum propagation [15].

4. An estimate of the exit wave leaving the specimen is given by the product of the illumination function and the transmission function of the specimen

$$\psi_j^n(\mathbf{r}) = P_j^n(\mathbf{r}) O^n(\mathbf{r}). \tag{4}$$

5. Propagate the exit wave to the detector plane via the Fresnel propagator [15] to give the diffraction pattern estimate

$$\Psi_j^n(\mathbf{u}) = \mathfrak{F} \left\{ \psi_j^n(\mathbf{r}) \exp\left(\frac{i\pi}{\lambda z} \mathbf{r}^2 \right) \right\}. \tag{5}$$

   Here $\mathfrak{F}$ represents Fourier transform, λ is the wavelength of the source and z is the distance between the specimen and the detector.

6. Apply the modulus constraint [16] and propagate back to the specimen, giving an updated exit wave

$$\hat{\psi}_j^n(\mathbf{r}) = \mathfrak{F}^{-1} \left\{ \sqrt{I_j(\mathbf{u})} \frac{\Psi_j^n(\mathbf{u})}{|\Psi_j^n(\mathbf{u})|} \right\} \exp\left(- \frac{i\pi}{\lambda z} \mathbf{r}^2 \right). \tag{6}$$

   Here $\Im^{-1}$ represents inverse Fourier transform.

7. Update the specimen and illumination functions using the newly-developed regularized PIE (rPIE) algorithm [17], which has been demonstrated to have an improved convergence rate over the ePIE algorithm [18],

$$\hat{P}_j^n(\mathbf{r}) = P_j^n(\mathbf{r}) + \frac{O^{n*}(\mathbf{r}) \left[\hat{\psi}_j^n(\mathbf{r}) - \psi_j^n(\mathbf{r}) \right]}{(1 - \alpha_P)|O^n(\mathbf{r})|^2 + \alpha_P |O^n(\mathbf{r})|^2_{\max}}. \tag{7}$$

$$O^{n+1}(\mathbf{r}) = O^n(\mathbf{r}) + \frac{P_j^{n*}(\mathbf{r}) \left[\hat{\psi}_j^n(\mathbf{r}) - \psi_j^n(\mathbf{r}) \right]}{(1 - \alpha_O)|P_j^n(\mathbf{r})|^2 + \alpha_O |P_j^n(\mathbf{r})|^2_{\max}}. \tag{8}$$

   Here $*$ represents complex conjugate, and α_P and α_O are two constants that can tune the convergence of the algorithm. For all the reconstructions demonstrated here, we used $\alpha_P = 0.5$ and $\alpha_O = 0.2$.

8. Propagate the updated illumination function back to the aperture and remove the tilted plane wave to give an updated estimate of the aperture and diffuser function

$$A^{n+1}(\mathbf{r}) = \wp_{\triangle z}^{-1} \Big\{ \hat{P}_j^n(\mathbf{r}) \Big\} \Gamma_j^*(\mathbf{r}). \tag{9}$$

9. Repeat step (3) to (8) until a preset convergence condition is fulfilled - either a fixed number of iterations or stagnation of an error metric.

We used a USAF resolution target to characterize and assess the performance of the proposed imaging method. The LED matrix used consisted of 8×8 LEDs with a separation of 8mm. A circular aperture of 150μm was placed downstream of the LED array, at a distance of 400mm. The aperture was covered by a plastic tape that acted as a diffuser. Following the aperture was the specimen (i.e. the resolution target) and the separation between them was about 1mm. A CCD camera (an AVT Pike F421B, with 2048×2048 pixels, each of $7.4\mu\text{m}^2$) was put behind the specimen at a distance of 22mm. According to this geometry, the angle difference between adjacent LEDs was about 0.02 rad and the separation of adjacent illumination functions in the specimen plane was about 20μm. 64 diffraction patterns were captured (one per LED), each binned by a factor of 4.

300 iterations of the procedure described in Section 2 gave the results shown in Fig. 2. The specimen modulus reconstruction is blurred and so is the aperture modulus reconstruction. We determined that this was caused by the low coherence condition of the experiment, which we will discuss later in detail. The specimen phase reconstruction also has an unrealistic curvature. We determined that this resulted from incorrect angle calibration of the LEDs in step (1) of our procedure; the phase curvature, acting like a lens, can compensate for errors in the illumination angles to some extent during the reconstruction.

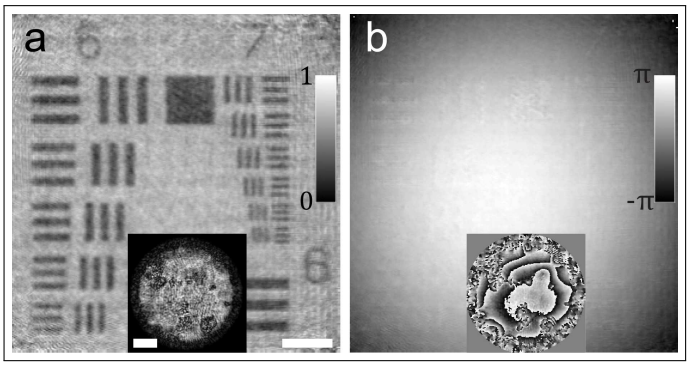

Fig. 2. The experimental reconstructions. (a) Moduli and (b) phases of the specimen and the aperture (inset). The scale bars indicate a length of 40μm.

3. ALGORITHM MODIFICATIONS TO HANDLE CHALLENGING EXPERIMENTAL CONDITIONS

In this section, we address the experimental issues with our setup one by one, and show how the diversity of the ptychographic data means that each source of error can be accommodated by a suitable adjustment to the basic algorithm presented in the previous section.

A. LED angle correction

The first problem we faced was that the accuracy of the cross correlation in step (1) was low, because it was carried out using the datasets measured with the specimen in the beam. Furthermore, the low coherence condition smooths the diffraction patterns, which also compromises the accuracy of the cross correlation. Fortunately, the accuracy can be improved by cross-correlating the measured diffraction patterns and their corresponding estimates calculated during the reconstruction, as given by

$$\triangle\mathbf{v}_j^n = \max_{\triangle\mathbf{v}}\left\{\sum_{\mathbf{u}} I_j(\mathbf{u})\left|\Psi_j^n(\mathbf{u}+\triangle\mathbf{v})\right|^2\right\}. \quad (10)$$

Here $\triangle\mathbf{v}_j^n$ is the correction of $\triangle\mathbf{u}_j$ for the jth LED at the nth iteration and the correction is given as

$$\triangle\mathbf{u}_j^{n+1} = \triangle\mathbf{u}_j^n + \triangle\mathbf{v}_j^n. \quad (11)$$

This correction step is implemented after step (5). Then for the next iteration, step (2) will use the updated $\triangle\mathbf{u}_j^{n+1}$ to generate the plane waves.

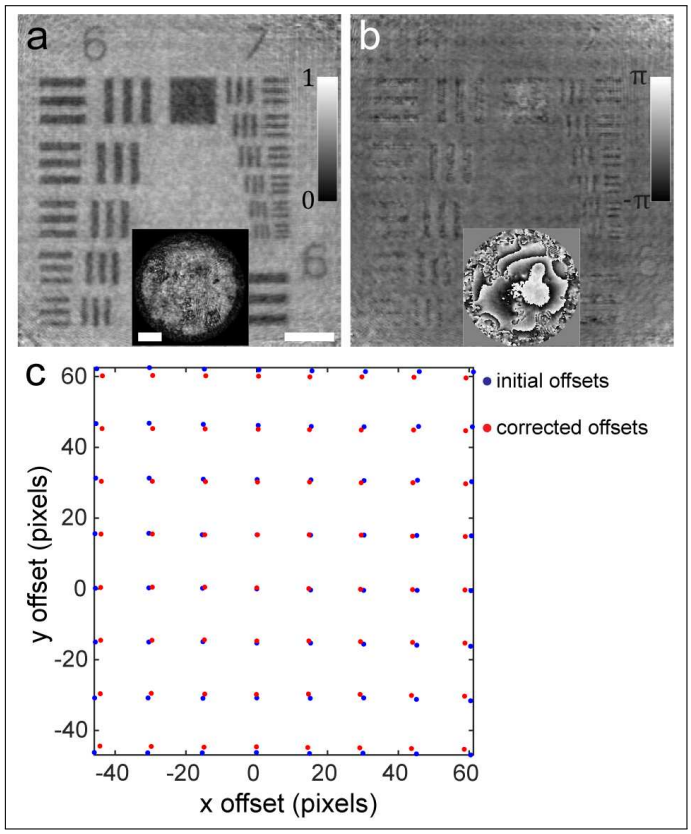

Fig. 3. The experimental reconstructions with angle correction. (a) Moduli and (b) phases of the specimen and the aperture (inset). (c) The offsets of the diffraction patterns before (blue points) and after (red points) the angle correction. The scale bars indicate a length of 40μm.

With the addition of this angle correction step, the reconstruction was repeated using the same resolution target test data. Again, 300 iterations were carried out. For the first 200 iterations, a flat phase constraint needs to be imposed, i.e. the phase of the specimen is forced to stay flat. This is because certain combinations of LED angles and specimen phase curvatures cause local minima that impede convergence. The flat phase constraint prevents these local minima and makes sure the algorithm converges to the true solution. It should be noted that this angle calibration only needs to be implemented once and that the following experiments can then use the calibrated angles. The reconstruction results after angle correction are shown in Fig. 3. The obvious difference, compared with the results shown

in Fig. 2, is the flat specimen phase reconstruction here, although the image is still very noisy.

B. Temporal coherence

Our initial reconstruction assumed that the illumination in our experiment was perfectly coherent. In fact, the LEDs did not have particularly good coherence. To show this, Figs. 4a and 4b show extracts from diffraction patterns recorded using one of the LEDs and a diode laser ($\lambda = 635$nm). The blurred speckles with low-contrast in Fig. 4a clearly indicate the low coherence of the LEDs, which is the result of the wide spectral bandwidth and the large spatial extent of the LEDs.

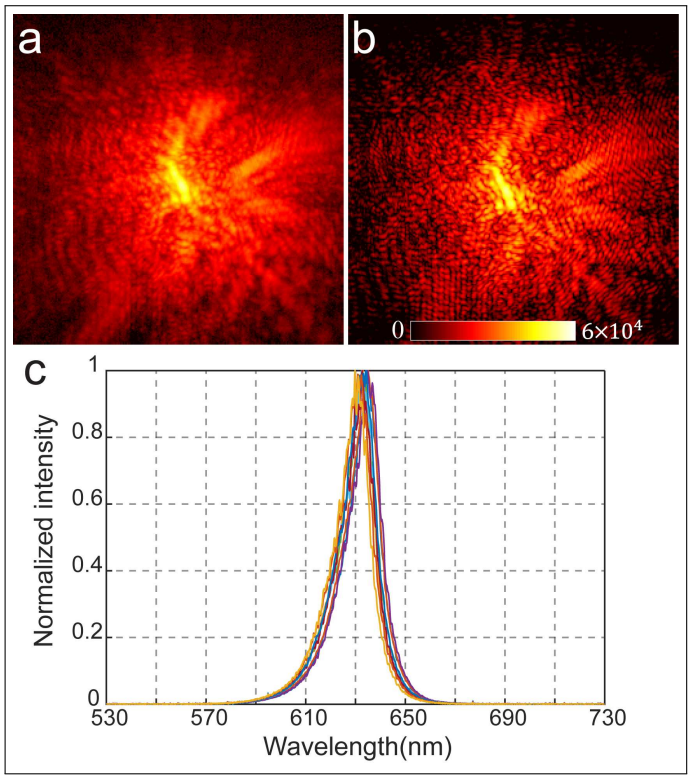

Fig. 4. The coherence property of the experiment. The measured diffraction pattern from (a) one of the LEDs and (b) a diode laser. (c) The measured spectra of 10 randomly chosen LEDs.

We randomly picked 10 LEDs and measured their frequency spectra, as plotted in Fig. 4c. Not surprisingly, they have rather wide bandwidths. We can use multicolor ptychography [19] to account for this partial temporal coherence, but given the limited number of measured diffraction patterns it would be very challenging to do so. Instead, we can make use of the measured spectra and account for low temporal coherence within the algorithm. Excepting some small offsets, the measured spectral distributions from the 10 different LEDs are very similar. As a result, we used the average distribution of the 10 measured spectra for all the LEDs. Supposing the specimen is non-dispersive, the diffraction patterns from different wavelengths are scaled copies of each other [20]. We used the central wavelength $\bar{\lambda} = 632.8$nm of the average spectrum to calculate the estimate of the diffraction pattern intensity $I_{\bar{\lambda}}(\mathbf{u}) = |\Psi_{\bar{\lambda}}(\mathbf{u})|^2$. Then the intensity corresponding to a different wavelength λ is calculated by mapping $I_{\bar{\lambda}}(\mathbf{u})$ onto a scaled coordinate as

$$I_{\lambda}(\mathbf{u}) = I_{\bar{\lambda}}\left(\frac{\lambda}{\bar{\lambda}}\mathbf{u}\right). \tag{12}$$

A weighted sum of all the intensities from different wavelengths then gives an estimate of the intensity caused by the low temporal coherence

$$I^{\text{est}}(\mathbf{u}) = \int \xi_{\lambda} I_{\lambda}(\mathbf{u}) \mathrm{d}\lambda. \tag{13}$$

The weighting factor ξ_{λ} is basically the relative contribution of the corresponding wavelength and it is given by the average spectrum. For the following reconstructions, 30 equidistant points on the average spectrum between 580nm and 660nm were used to account for the low temporal coherence. Accordingly, the modulus constraint in step (6) was modified as

$$\hat{\psi}^n_{j,\bar{\lambda}}(\mathbf{r}) = \mathfrak{F}^{-1}\left\{\sqrt{I^{\text{mea}}_j(\mathbf{u})}\frac{\Psi^n_{j,\bar{\lambda}}(\mathbf{u})}{I^{\text{est}}_j(\mathbf{u})}\right\}\exp\left(-\frac{i\pi}{\bar{\lambda}z}\mathbf{r}^2\right). \tag{14}$$

Here $I^{\text{mea}}(\mathbf{u})$ represents the diffraction pattern intensity measured by the detector.

Having implemented the angle correction and temporal coherence additions, the algorithm was run again for 300 iterations. The results are shown in Fig. 5. The improvements in both the specimen reconstruction and the aperture reconstruction are significant: the background is much cleaner and the features are much sharper.

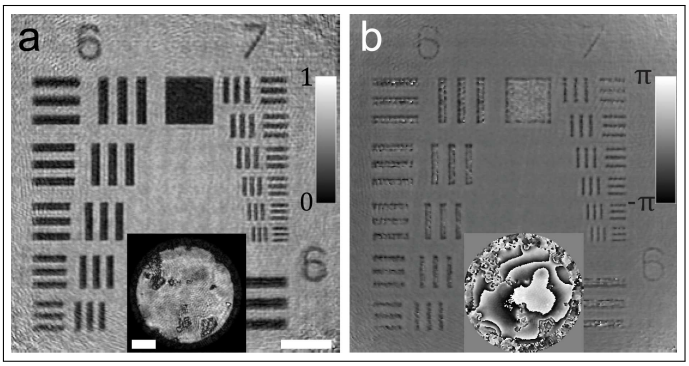

Fig. 5. The experimental reconstructions after taking into account of both angle correction and temporal coherence. (a) Moduli and (b) phases of the specimen and the aperture (inset). The scale bars indicate a length of 40μm.

C. Spatial coherence

The spatial coherence of the experiment was also limited because of the relatively large size of the LEDs in the matrix. To test the degree of spatial coherence, we changed the LED-aperture distance and observed the reduction in fringe visibility that this caused. Figure 6 shows the measured diffraction patterns with two different LED-aperture distances (300mm and 200mm). Together with the diffraction pattern shown in Fig. 4a (where the distance was 400mm), it is not difficult to see that the diffraction patterns have lower contrast (i.e. worse spatial coherence) when shorter LED-aperture distances are used, which demonstrates that the experiment had a limited spatial coherence.

The use of incoherent modes (or mixed states) is the common way to solve this problem of limited spatial coherence [21][22].

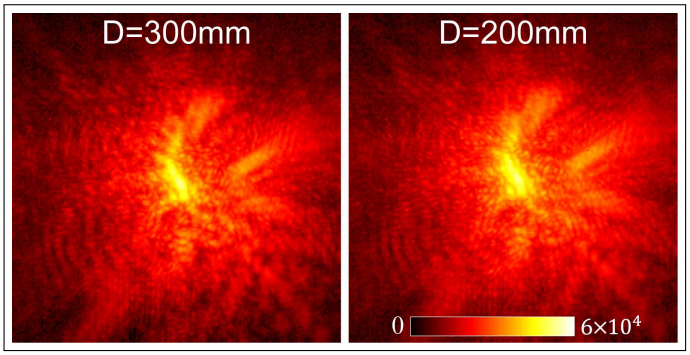

Fig. 6. Diffraction patterns measured at different LED-aperture distances.

Here we modified the rPIE algorithm to operate using incoherent modes. Following the derivation in ref. [17] and the supplementary materials of ref. [21], the modified cost function for the jth LED with incoherent modes is:

$$E_j = \sum_{k,j}\sum_{\mathbf{r}} \left| P_j^{(k)\prime}(\mathbf{r}) O^{(l)}(\mathbf{r}) - \hat{\psi}_j^{(k,l)}(\mathbf{r}) \right|^2 + \sum_{k,j} u(\mathbf{r}) \left| P^{(k)\prime}(\mathbf{r}) - P^{(k)}(\mathbf{r}) \right|^2. \tag{15}$$

Here k and l are the indices of the incoherent modes for the illumination and the specimen respectively. Setting the gradient of the cost function to zero and using the following choice of

$$u(\mathbf{r}) = \alpha \left\{ \left[\sum_l \left| O^{(l)}(\mathbf{r}) \right|^2 \right]_{\max} - \sum_l \left| O^{(l)}(\mathbf{r}) \right|^2 \right\}, \tag{16}$$

we obtain the corresponding update function for the illumination modes as

$$P_j^{(k)\prime}(\mathbf{r}) = P_j^{(k)}(\mathbf{r}) + \frac{\sum_l O^{(l)*}(\mathbf{r}) \left[\hat{\psi}_j^{(k,l)}(\mathbf{r}) - \psi_j^{(k,l)}(\mathbf{r}) \right]}{(1-\alpha_P) \sum_l \left| O^{(l)}(\mathbf{r}) \right|^2 + \alpha_P \left[\sum_l \left| O^{(l)}(\mathbf{r}) \right|^2 \right]_{\max}}. \tag{17}$$

Likewise, the update function for the specimen modes is given by

$$O^{(l)\prime}(\mathbf{r}) = O^{(l)}(\mathbf{r}) + \frac{\sum_k P_j^{(k)*}(\mathbf{r}) \left[\hat{\psi}_j^{(k,l)}(\mathbf{r}) - \psi_j^{(k,l)}(\mathbf{r}) \right]}{(1-\alpha_O) \sum_k \left| P_j^{(k)}(\mathbf{r}) \right|^2 + \alpha_O \left[\sum_k \left| P_j^{(k)}(\mathbf{r}) \right|^2 \right]_{\max}}. \tag{18}$$

Again, we implemented this modification to the algorithm and carried out a reconstruction using 4 illumination modes and 1 specimen mode. The specimen reconstructions are shown in Figs. 7a (modulus) and 7b (phase). The main illumination mode in the aperture plane (we will refer to it as the aperture mode reconstruction hereinafter) is also given in the inset for comparison. Compared to the results shown in Fig. 5, the reconstructions here (both the specimen and the aperture) are obviously much better. Figure 7c shows the four aperture modes together with their relative power in hue-saturation-value (HSV) colorscale: the color wheel depiction shows phase variations as changes in hue and modulus variations as changes in brightness.

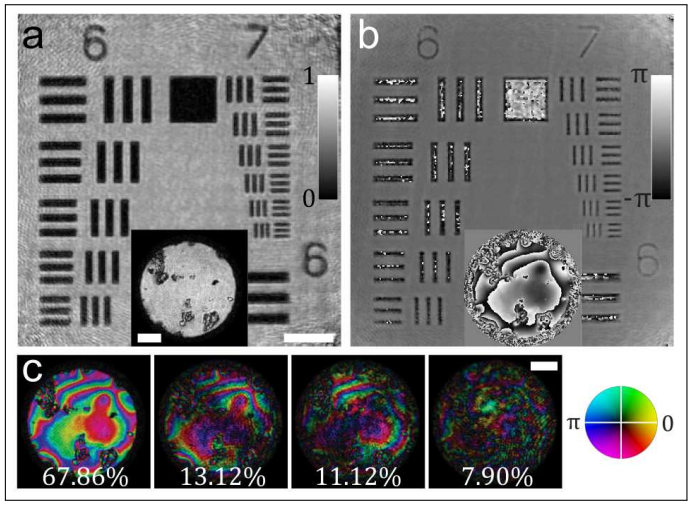

Fig. 7. The experimental reconstructions after taking into account of angle correction, temporal coherence and spatial coherence. (a) Moduli and (b) phases of the specimen and the main aperture mode (inset). (c) The four aperture modes in HSV colorscale together with their relative power. The scale bars indicate a length of 40μm.

D. Variance between the individual LEDs

The LEDs in the matrix are similar, so the algorithm has managed to get a reasonable reconstruction so far. However, small variances do exist between individual LEDs, for example in their brightness, orientation and coherence properties etc. These small variances can be taken into account using orthogonal probe relaxation (OPR) [23], which is equivalent to the principle component analysis (PCA) method [24]. This requires the algorithm to reconstruct a separate illumination function for each LED. Then the illumination functions are decomposed into a set of principal components (much less than the number of LEDs). Truncated singular value decomposition (tSVD) [25] was used to obtain the principal components as

$$[U, S, V] = \mathrm{tSVD}(P, n). \tag{19}$$

Here the columns of P are the vectorised illumination functions and n is the number of principle components. The columns of US are the principal components and the columns of V are the principal axes. The lower dimensional illumination functions $\hat{P}$ are linked by the principle components via a linear combination with different coefficients as

$$\hat{P} = USV^*. \tag{20}$$

Here $*$ represents the complex conjugate. $\hat{P}$ is then used for the next iteration of the reconstruction algorithm. These two operations (Eqs. (19) and (20)) need to be repeated for all the incoherent illumination modes. Here we used 4 principle components (i.e. $n = 4$) to our algorithm and ran a further 200 iterations, beginning from the reconstructions shown in Fig. 7. The results are shown in Fig. 8. It should be noted that the aperture reconstruction shown in the inset is the average of the main incoherent illumination mode in the aperture plane over all LEDs, because here each LED has independent illumination mode reconstructions. No major improvements can be observed from the specimen and the aperture reconstructions. However, with close examination of the zoom in figures (Figs.

8c and 8d) of the same specimen region from both reconstructions, we can see that the reconstruction has a somewhat more uniform and cleaner background when LED variance is considered. Moreover, the reconstruction error, which is calculated as the difference of the measured diffraction patterns and their according estimates [18], has an evident drop when OPR is applied, as shown in Fig. 8e. Figures 8f and 8g respectively show the four principle components (i.e. matrix US) and their linear coefficients (i.e. matrix V) for the main incoherent mode of the 64 different illumination functions. The fact that most of the power falls into one component and its corresponding (complex) coefficients for all illumination functions are very close indicates that the variance between individual LEDs is very small.

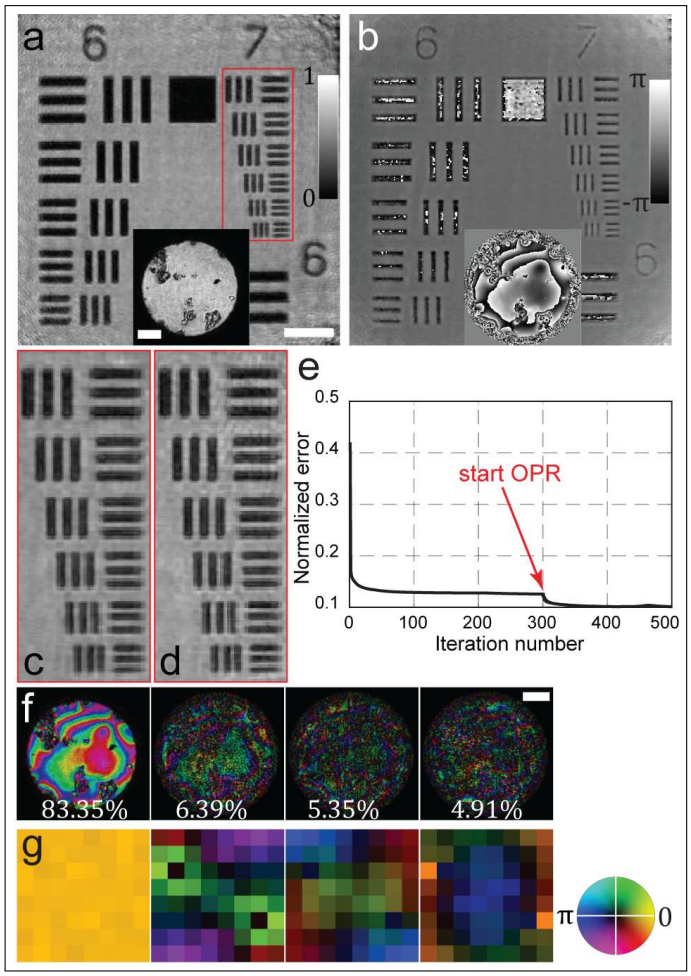

Fig. 8. The experimental reconstructions after taking into account of angle correction, temporal coherence, spatial coherence and LED variance. (a) Moduli and (b) phases of the specimen and the average of the main illumination mode in the aperture plane (inset). (c) The zoom in view of the area marked by the red rectangle in (a). (d) The zoom in view of the same area of the reconstruction shown in Fig. 7a. (e) The reconstruction error plot. (f) The four principle components and (g) their according linear coefficients for main incoherent mode of the 64 illumination functions in HSV colorscale. The scale bars indicate a length of 40μm.

4. DEMONSTRATION OF BIOLOGICAL SAMPLE

A microscope slide of stained human blood cells has also been imaged to demonstrate the performance of the proposed method. Because the whole imaging system remains the same, all the calibrated parameters - the LED angles, the incoherent illumination modes and the principle illumination components - can be re-used for the new specimen reconstruction. As a result, the reconstruction converges very fast. Figure 9 shows the quantitative reconstruction of the cells in HSV colorscale together with two optical microscope images of the cells using 10× and 20× objectives respectively. The proposed method has an imaging ability that is visually comparable with an optical microscope using a 20× objective. However, the important thing about the proposed method is that it does not rely on staining to provide the contrast, while the conventional optical microscope does. Therefore, applications like non-invasive live cell imaging are possible using the proposed imaging method.

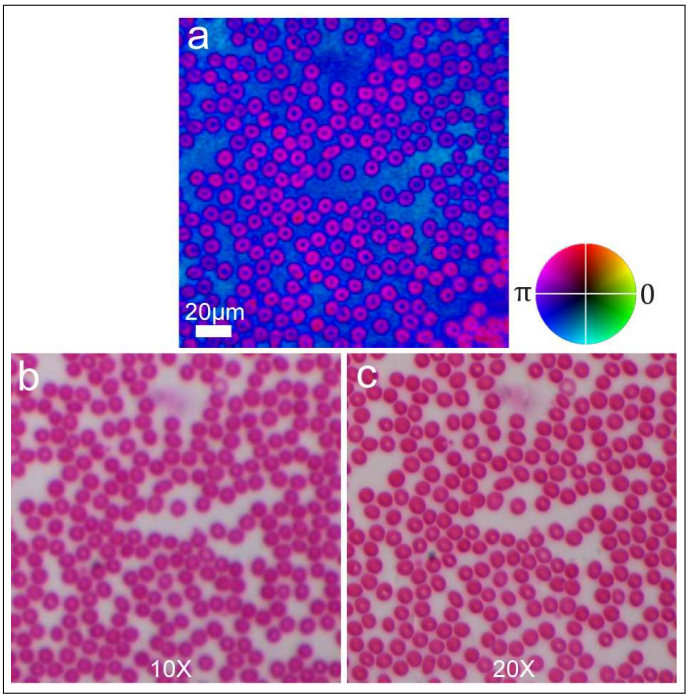

Fig. 9. Imaging demonstration of human blood cells. (a) The reconstruction result of the proposed method. (b) The optical microscope image using a 10× objective. (c) The optical microscope image using a 20× objective.

5. CONCLUSION AND DISCUSSION

In this paper, we have reported a lensless microscopic imaging method that is enabled by using a LED matrix and an aperture. No mechanic movement is involved during the imaging process, which is beneficial because: 1. it simplifies and reduces the cost of the imaging system without the need of a mechanic scan stage; 2. it speeds up the data acquisition process; 3. it avoids perturbing the specimen. Moreover, our setup uses a LED matrix instead of a laser as the illumination source, which further reduces the cost of the imaging system. The access to the quantitative phase information provided by the proposed imaging method, not only produces good contrast without labelling which is important for studying samples at their natural state

like live cell imaging [5], but also allows to perform quantitative analysis on the samples which could be made use of in optical metrology.

Because many of the assumptions of conventional ptychography do not apply to this new setup, a dedicated phase retrieval algorithm based on multislice ptychography has also been developed to produce the complex image of the specimen. This algorithm highlights the remarkable range of factors that the ptychographic scheme can successfully handle, from temporal and spatial partial coherence to variance between the individual LEDs in the matrix. This flexibility holds promise for other forms of microscopy. In electron ptychography [26], for example, the temporal and spatial coherence are limited and the illumination variance also exists because of lens instabilities. For Fourier ptychography [27], a lens-aided imaging method that also uses LED matrix, can also make use of the proposed reconstruction strategy to accommodate the imperfections of the LEDs.

Regarding the field of view of the proposed imaging method, this can be easily increased by using a larger aperture. For the LED matrix we used here, this will lead to lower spatial coherence, although LEDs with better coherence properties (and still very cheap) are commercially available. Bigger LED matrices (adding more LEDs) can also increase the field of view, but this would affect the resolution limit, which is fundamentally limited by the highest scattering angle of the diffraction pattern that is able to be captured by the detector.

Funding Information. Engineering and Physical Sciences Research Council (EPSRC) (EP/N019563/1).

Acknowledgement. The authors want to thank Tega Edo and Zhuoqun Zhang with their assistance in setting up the LED matrix.

REFERENCES

1. A. Greenbaum *et al.*, "Imaging without lenses: achievements and remaining challenges of wide-field on-chip microscopy," Nat. Methods **9**, 889 – 895 (2012).
2. P. Marquet *et al.*, "Digital holographic microscopy: a noninvasive contrast imaging technique allowing quantitative visualisation of living cells with subwavelength axial accuracy," Opt. Letts. **30**, 468 – 470 (2005).
3. F. Zernike, "Phase contrast, a new method for the microscopic observation of transparent objects," Physica **9**, 686 – 698 (1942).
4. G. Nomarski, "Microinterferometre differentiel a ondes polarisees," J. Phys. Radium **16**, S9 – S13 (1955).
5. J. Marrison, L. Raty, P. Marriott, and P. O'Toole, "Ptychography-a label free, high-contrast imaging technique for live cells using quantitative phase information," Scientific Reports **3**, 2369 (2013).
6. R. W. Gerchberg and W. O. Saxton, "PA practical algorithm for the determination of the phase from image and diffraction plane pictures," Optik **35**, 237–246 (1972).
7. J. R. Fienup, "Reconstruction of an object from the modulus of its fourier transform," Opt. letters **3**, 27–29 (1978).
8. J. R. Fienup, "Phase retrieval algorithms: a comparison," Appl. optics **21**, 2758–2769 (1982).
9. M. R. Teague, "Deterministic phase retrieval: a Green's function solution," J. Opt. Soc. Am. **73**, 1434–1441 (1983).
10. W. M. J. Coene, A. Thust, M. O. de Beeck, and D. Van Dyck, "Maximum-likelihood method for focus - variation image reconstruction in high resolution transmission electron microscopy," Ultramicroscopy **64**, 109–135 (1996).
11. P. Thibault *et al.*, "High-Resolution Scanning X-ray Diffraction Microscopy," Science **321**, 379 (2008).
12. P. F. Almoro *et al.* "Enhanced intensity variation for multiple-plane phase retrieval using a spatial light modulator as a convenient tunable diffuser," Optics letters **10**, 2161–2164 (2016).
13. P. Li *et al.* "Multiple mode x-ray ptychography using a lens and a fixed diffuser optic," Journal of Optics **18**, 054008 (2016).
14. A. M. Maiden, M. J. Humphry, and J. M. Rodenburg, "Ptychographic transmission microscopy in three dimensions using a multi-slice approach," JOSA A **29**, 1606–1614 (2012).
15. J. W. Goodman, Fresnel and Fraunhofer Diffraction in *Introduction to Fourier Optics* (ed. Goodman, J. W.) chapter 4 (Roberts & Company, 2005).
16. P. Thibault, M. Dierolf, O. Bunk, A. Menzel, and F. Pfeiffer, "Probe retrieval in ptychographic coherent diffractive imaging," Ultramicroscopy **109**, 338–343 (2009).
17. A. Maiden, D. Johnson, and P. Li, "Further improvements to the ptychographical iterative engine," Optica **4**, 736–745 (2017).
18. M. Maiden, and J. M. Rodenburg, "An improved ptychographical phase retrieval algorithm for diffractive imaging," Ultramicroscopy **109**, 1256–1262 (2009).
19. D. J. Batey, D. Claus, and J. M. Rodenburg, "Information multiplexing in ptychography," Ultramicroscopy **138**, 13–21 (2014).
20. B. Abbey *et al.*, "Lensless imaging using broadband X-ray sources," Nat. Photonics **5**, 420–424 (2011).
21. P. Thibault, and A. Menzel, "Reconstructing state mixtures from diffraction measurements," Nature **494**, 68–71 (2013).
22. P. Li, T. Edo, D. Batey, J. Rodenburg, and A. Maiden, "Breaking ambiguities in mixed state ptychography," SOptics Express **24**, 9038–9052 (2016).
23. M. Odstrcil *et al.*, "Ptychographic coherent diffractive imaging with orthogonal probe relaxation," Optics Express **24**, 8360–8369 (2016).
24. S. Wold, K. Esbensen, and P. Geladi, "Principal component analysis," Chemometrics and Intelligent Laboratory Systems **2**, 37–52 (1987).
25. N. Halko, P. G. Martinsson, Y. Shkolnisky, and M. Tygert, "An algorithm for the principal component analysis of large data sets," SIAM J. Sci, Comput. **33**, 2580–2594 (2011).
26. A. M. Maiden, M. C. Sarahan, M. D. Stagg, S. M. Schramm, and M. J. Humphry "Quantitative electron phase imaging with high sensitivity and an unlimited field of view," Scientific Reports **5**, 14690 (2015).
27. G. Zheng, R. Horstmeyer, and C. Yang "Wide-field, high-resolution Fourier ptychographic microscopy," Nature Photonics **7**, 739–745 (2013).